Two-dimensional polyaniline (C₃N) from carbonized organic single crystals in solid state

Javeed Mahmood[a,1], Eun Kwang Lee[a,b,1], Minbok Jung[c], Dongbin Shin[d], Hyun-Jung Choi[a], Jeong-Min Seo[a], Sun-Min Jung[a], Dongwook Kim[d], Feng Li[a], Myoung Soo Lah[d], Noejung Park[d,2], Hyung-Joon Shin[c,2], Joon Hak Oh[b,2], and Jong-Beom Baek[a,2]

[a]Center for Dimension-Controllable Organic Frameworks, School of Energy and Chemical Engineering, Ulsan National Institute of Science and Technology, Ulsan 44919, South Korea; [b]Department of Chemical Engineering, Pohang University of Science and Technology, Pohang 37673, South Korea; [c]School of Materials Science and Engineering, Ulsan National Institute of Science and Technology, Ulsan 44919, South Korea; and [d]School of Natural Science, Ulsan National Institute of Science and Technology, Ulsan 44919, South Korea

The formation of 2D polyaniline (PANI) has attracted considerable interest due to its expected electronic and optoelectronic properties. Although PANI was discovered over 150 y ago, obtaining an atomically well-defined 2D PANI framework has been a longstanding challenge. Here, we describe the synthesis of 2D PANI via the direct pyrolysis of hexaaminobenzene trihydrochloride single crystals in solid state. The 2D PANI consists of three phenyl rings sharing six nitrogen atoms, and its structural unit has the empirical formula of C_3N. The topological and electronic structures of the 2D PANI were revealed by scanning tunneling microscopy and scanning tunneling spectroscopy combined with a first-principle density functional theory calculation. The electronic properties of pristine 2D PANI films (undoped) showed ambipolar behaviors with a Dirac point of −37 V and an average conductivity of 0.72 S/cm. After doping with hydrochloric acid, the conductivity jumped to 1.41×10^3 S/cm, which is the highest value for doped PANI reported to date. Although the structure of 2D PANI is analogous to graphene, it contains uniformly distributed nitrogen atoms for multifunctionality; hence, we anticipate that 2D PANI has strong potential, from wet chemistry to device applications, beyond linear PANI and other 2D materials.

polyaniline | two-dimensional | solid-state reaction | C₃N | nitrogenated graphene

Although one-dimensional (1D) linear polyaniline (PANI) was discovered in 1834 (1), the word PANI was first coined in 1947 (2), and PANI garnered immense attention from the scientific community due to its intrinsically conducting nature (3). During the last three decades, PANI has been one of the most extensively studied conducting polymers because of its simple synthesis, low cost, high conductivity, environmental stability, and doping chemistry (4, 5). Linear PANI has found broad applicability in rechargeable batteries (6), electromagnetic shielding (7), nonlinear optics (8), light-emitting devices (9), sensors (10), field effect transistors (11), erasable optical information storage (12), membranes (13), digital memory devices (14), electrochemical capacitors (15), electrochromic devices (16), antistatic and anticorrosion coatings (17), fuel cells (18), solar cells (19), and radar absorbing materials (20). Supramolecular PANI nanostructures such as 0D (nanospheres) (21), 1D [nanofibers (22), nanowires (23), nanorods (24), and nanotubes (25)], 2D [nanobelts (26) and nanosheets (27)], cyclic, spiral, and complex nanostructures have also been reported (28). However, due to the mechanistic complexity of aniline polymerization, the atomic-scale control of PANI structure has not yet been realized (28). Together with the recent discovery of all-carbon-based 2D graphene and its promising potentials (29), 2D network polymers are galvanizing a new wave of research in the scientific community (30). Here, we, for the first time to our knowledge, report the synthesis of real 2D PANI framework from direct pyrolysis of organic single crystals, hexaaminobenzene trihydrochloride (HAB), at 500 °C. This synthetic methodology could serve as a straightforward way for the design and synthesis of other new 2D layered materials with many potential applications, from wet chemistry to devices.

Results and Discussion

The key building block, HAB, as a monomer with six functional groups (M6), was synthesized in a pure crystalline form (Fig. 1A and *SI Appendix*, Fig. S1) (31). It was observed that the HAB single crystals pyrolyze before melting and maintain their well-defined, needle-like crystal morphologies even after pyrolysis at 500 °C. The pure HAB crystals have a well-defined hexagonal morphology (Fig. 1 B−D and *SI Appendix*, Figs. S2 and S3), which is maintained even after annealing at 500 °C (Fig. 1 E−G and *SI Appendix*, Figs. S4 and S5). These results suggest that HAB single crystals could be directly pyrolyzed into highly stable, rigid hexagonal rods. The pyrolyzed HAB crystals, which are up to a few millimeters long, have a rod-like hexagonal structure. High-resolution SEM images reveal a more layered graphitic structure and a highly wrinkled morphology (Fig. 1G and *SI Appendix*, Fig. S4), which is attributed to the 2D sheet-like appearance of the 2D PANI framework. Hence, we investigated the mechanism underlying the pyrolysis of HAB single crystals. The transformation of HAB crystals into a 2D layered PANI structure should involve releases of ammonium chloride (NH_4Cl) and ammonia (NH_3) via a concerted mechanism (Fig. 1A and *SI Appendix*, Fig. S6).

Significance

Two-dimensional (2D) polyaniline (PANI) has been realized for the first time, to our knowledge, by direct solid-state reaction of organic single crystals. The 2D PANI framework consists of six nitrogen atoms that periodically surround a phenyl ring. Pristine 2D PANI (undoped) has electrical conductivity of 0.72 S/cm, which is 10^{10} times higher than its linear analog (undoped, 6.28×10^{-11} S/cm). When it is doped by hydrochloric acid (HCl), its conductivity jumps to almost 1,960 times (1.41×10^3 S/cm). Due to its highest conductivity among organic materials, we very strongly believe that this well-defined 2D PANI and its heterogeneity with C and N elements will open up a new research field of layered 2D materials beyond linear PANI and other organic/inorganic 2D materials.
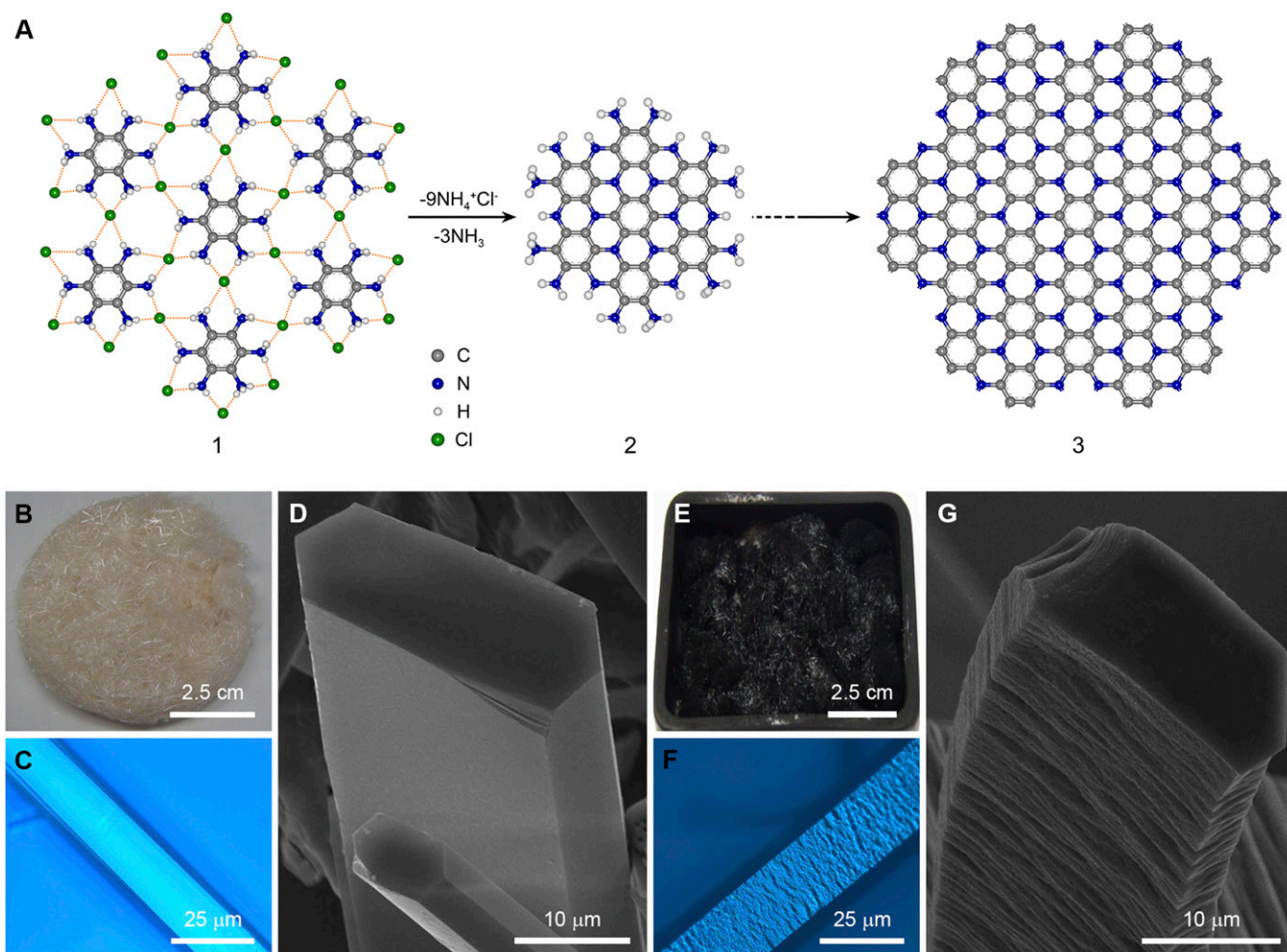
Fig. 1. Schematic representation of 2D PANI formation. (*A*) Single-crystal X-ray packing structure of HAB (structure 1); structure of 2D PANI unit with edge groups (C₃NH, structure 2), and the spontaneous transformation of HAB crystal unit into the 2D PANI structure (structure 3). Morphology changes of HAB crystals into 2D PANI frameworks. (*B*) Digital photograph of HAB crystals on butter paper. (*C*) Optical microscopy image of a needle-like HAB crystal before annealing. (*D*) SEM image of an HAB single crystal before annealing. (*E*) Digital image of HAB after annealing at 500 °C. (*F*) Optical microscopy image of 2D PANI crystal after annealing at 500 °C. (*G*) SEM image of a 2D PANI single crystal after annealing.

To confirm the unusual chemistry of the 2D network-forming reaction and the stability of the resulting product, the pure HAB crystals were subjected to thermogravimetric analysis (TGA) (Fig. 2*A*) under an argon atmosphere. At ~250 °C, the HAB single crystal (Fig. 2*A*, *Left Inset*), which is considered to be a hexa-functional (M6) monomer, undergoes an endothermic weight loss of 15%. This weight loss is attributed to the partial evaporation of bound hydrochloric acid (HCl) and water. A highly exothermic weight loss of 42% is observed at ~325 °C, indicating that new covalent bonds and a stable network structure are formed (Fig. 2*A*, *Right Inset*), as the remaining ammonium chloride (NH₄Cl) and ammonia (NH₃) molecules are released from the structure. The release of ammonium chloride and ammonia was confirmed using chemical methods (*SI Appendix*, Fig. S7; the detailed test method and corresponding discussion are described). The formation energy per repeating unit of the 2D PANI structure ($C_6N_6H_{15}Cl_3 \rightarrow C_6N_2 + 3NH_4Cl + NH_3$) was calculated to be −2.03 eV, using first-principle density functional theory (DFT) calculations (*SI Appendix*, Fig. S8), demonstrating the driving force of reaction and stability of the formed product. Thus, the process is assumed to spontaneously produce a covalently bonded 2D PANI network structure. In addition, the product exhibits good thermal stability in both

nitrogen (Fig. 2*B*) and air (*SI Appendix*, Fig. S9), suggesting the formation of stable 2D PANI network structures.

The elemental composition determined using the different techniques is very close to the calculated value (*SI Appendix*, Table S1). The empirical formula of the 2D PANI is C₃N for the core repeat unit (structure 3, Fig. 1*A*). When bulk molecule with the edge amine functional groups is taken into account, the empirical formula is C₃NH (structure 2, Fig. 1*A*; structure 7, *SI Appendix*, Fig. S6). This interesting 2D PANI structure was further verified using solid-state carbon NMR (¹³C-NMR) measurements, showing only two peaks in the spectrum (Fig. 2*C*). The peak at 150.80 ppm is attributed to the carbon atoms attached to tertiary nitrogen in the basal plane of 2D PANI framework (dark blue dot, Fig. 2*C*, *Inset*). The peak at 126.02 ppm is assigned to the carbon atoms covalently bonded to primary or secondary amine groups at the edges of 2D PANI framework (dark yellow dot, Fig. 2*C*, *Inset*).

The chemical composition and bond nature of 2d PANI were probed using X-ray photoelectron spectroscopy (XPS). The XPS survey spectrum contains only C 1s, N 1s, and O 1s peaks, and no other impurities are observed (Fig. 2*D*). The high-resolution C 1s spectrum can be deconvoluted into three peaks at 284.6, 285.6 and 288.5 eV (*SI Appendix*, Fig. S10*A*). The peaks at 284.6 and 285.6 eV
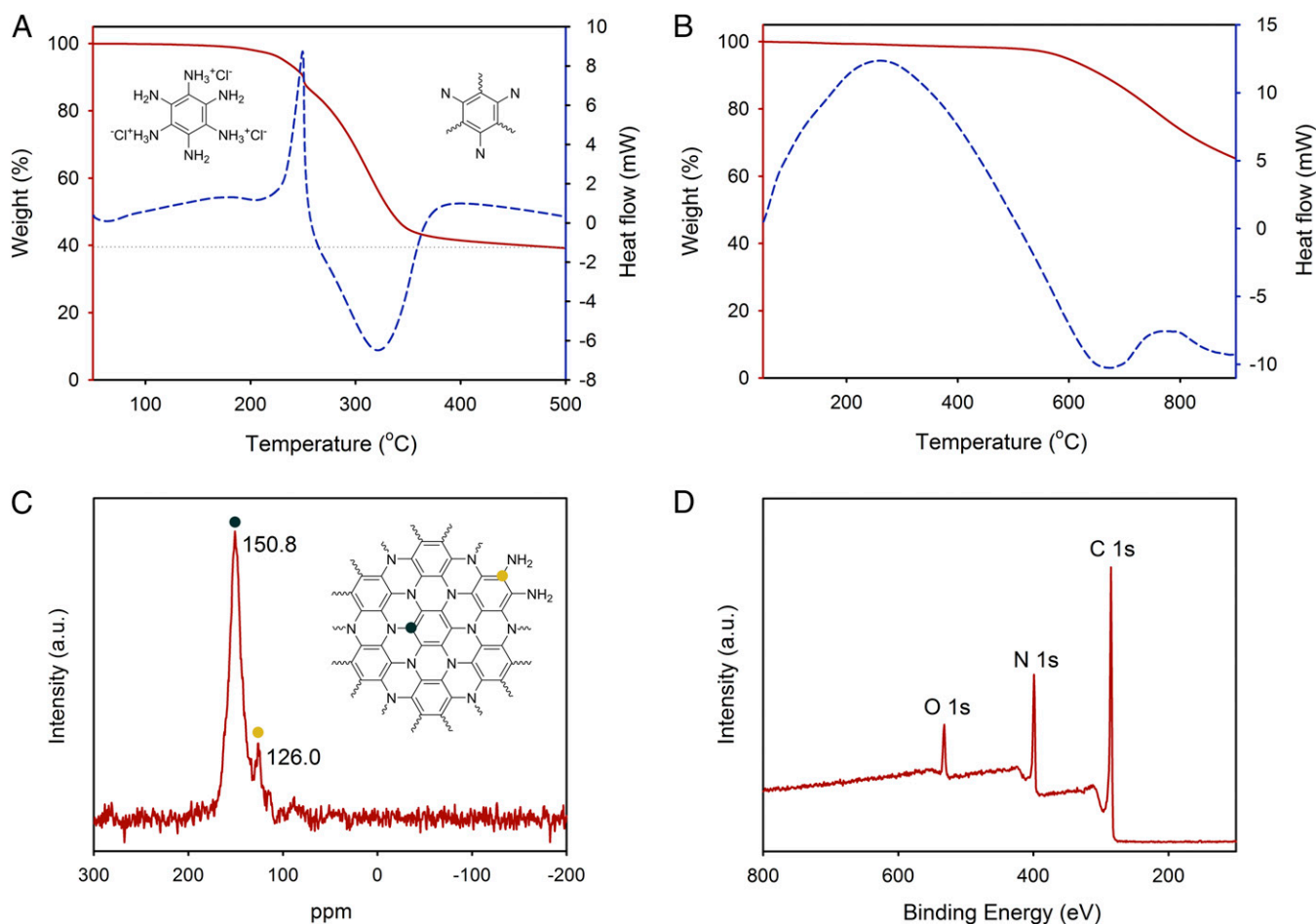
Fig. 2. Characterizations of the 2D PANI structures. (*A*) TGA thermogram obtained from an HAB single crystal with a ramping rate of 10 °C/min in argon. (*B*) TGA thermogram obtained from a 2D PANI framework with a ramping rate of 10 °C/min in argon. TGA thermogram in air is presented in *SI Appendix*, Fig. S9. (*C*) Solid-state ^{13}C magic-angle spinning NMR spectrum of 2D PANI framework showing only two carbon peaks. (*D*) XPS survey spectrum of 2D PANI framework. Its high-resolution XPS spectra are presented in *SI Appendix*, Fig. S10.

are assigned to *sp*^{2} *C*−*C* and *sp*^{2} *C*−*N*, respectively, in the 2D PANI framework, whereas the minor peak at 288.5 eV is attributed to *C*−NH$_2$ at the edges. The N 1s spectrum has two peaks, at 398.6 eV and 400.6 eV due to *sp*^{2} C$_2$−*N*H and *sp*^{2} C$_3$−*N*, respectively (*SI Appendix*, Fig. S10*B*). The small oxygen content (O 1s) in the structure can be assigned to physically adsorbed molecular oxygen and water due to the polar nature of material (*SI Appendix*, Fig. S10*C*). The powder X-ray diffraction (PXRD) from the 2D PANI reveals three major peaks (2θ) at 12.8°, 26.12°, and 44.7°, with corresponding *d* spacing of 6.87 Å, 3.40 Å, and 2.02 Å (*SI Appendix*, Fig. S11). The peak at 26.12° is associated with interlayer *d* spacing (3.40 Å) of the 2D PANI. The experimental PXRD result is in good agreement with the simulated XRD pattern after Pawley refinement (*SI Appendix*, Table S2).

To resolve the atomic-level structure of the 2D PANI framework, we performed scanning tunneling microscopy (STM) (SPECS JT-STM). HAB molecules were deposited in situ on a clean Cu(111) single crystal by thermal evaporation at 600 K followed by annealing for 5 min. All of the STM experiments were performed under ultrahigh vacuum (UHV) at a low temperature (77 K). The 2D PANI framework has a well-ordered triangular structure (Fig. 3*A*) with the dot-to-dot distance of 442 ± 16 pm (Fig. 3*B*). To examine the electronic structure of 2D PANI, scanning tunneling spectroscopy (STS) was performed using the lock-in detection technique. Two prominent peaks were observed, at −1.0 eV and 1.6 eV in the valence band and conduction band regions, respectively (Fig. 3*C*),

which is in good agreement with the electrochemically determined highest occupied molecular orbital (HOMO)-lowest occupied molecular orbital (LUMO) gap of 2.67 eV (*SI Appendix*, Fig. S12 *A* and *B*). The measurement of the electrochemical HOMO−LUMO gap from the starting HAB molecules was not possible because of the instability of HAB in the measuring condition (*SI Appendix*, Fig. S12*C*), indicating that 2D PANI structures are distinctly different from those of self-assembled HAB molecular crystals without pyrolysis.

First-principles DFT calculations were performed to analyze the STM image and to determine the electronic structure. To produce the calculated STM image, the Kohn−Sham charge density was integrated from the Fermi level to 1.1 eV below the Fermi level. The theoretical lattice constant is 475 pm (Fig. 3*D*), which is well matched with experimental observation (Fig. 3*A*). The band structure along the symmetry lines in the Brillouin zone and the projected density of electronic states (PDOS) are shown in Fig. 3 *E* and *F*, respectively. Gradient-corrected DFT calculations show that the 2D PANI framework has a nonzero finite density of states near the Fermi level, in agreement with the STS measurement (Fig. 3*C*). The valence band maximum and conduction band minimum are both derived from the carbon and nitrogen *p$_z$* orbitals. The detailed electronic structures are described in *SI Appendix*, Fig. S13. The conduction band minimum states closely resemble the electronic structures of benzene rings bridged by nitrogen atoms.
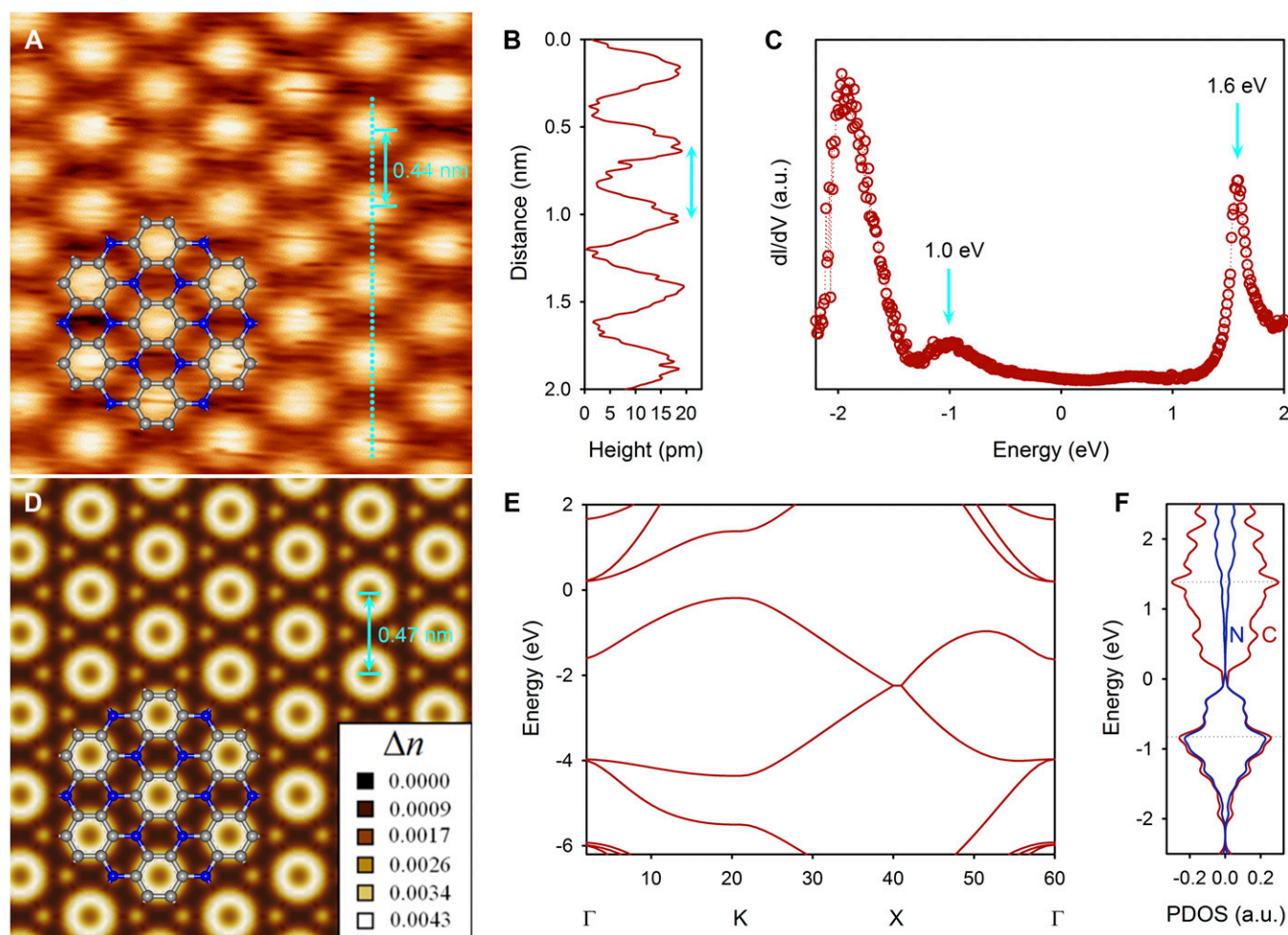
Fig. 3. STM and theoretical studies of the 2D PANI structure. (*A*) STM image of a 2D PANI framework (2.5×2.5 nm^2, Vs. = -1.1V, I_t = 1.0 nA). *Inset* structure represents C$_3$N repeating unit with carbon atom (gray ball) and nitrogen atom (blue ball). (*B*) Topographic height profile along the cyan dot line marked in *A*. (*C*) Differential conductance (*dI/dV*) spectrum of a 2D PANI framework. (*D*) Simulated STM image with superimposed structure of C$_3$N repeating unit. (*E*) Electronic band structure. (*F*) PDOS of the carbon (dark red) and nitrogen (dark blue) atoms.

To elucidate the electrical properties, field-effect transistors (FETs) were fabricated using 2D PANI flakes as the active layer. The 2D PANI flakes were isolated onto Si wafer with 300-nm-thick SiO$_2$ by using polydimethylsiloxane (PDMS) stamping from the prepared films (32). Fig. 4*A* is a typical optical image of the FET based on a 2D PANI flake. Source and drain electrodes were deposited with the thermal evaporation of Cr (4 nm) and Au (40 nm) and followed by e-beam lithography (channel length = 500 nm). The electrical properties of 10 FETs based on 2D PANI flakes were characterized (Fig. 4*A* and *SI Appendix*, Fig. S14). Atomic force microscopy (AFM) analysis of 2D PANI flake positioned on a white square (Fig. 4*A*) disclosed that the average thickness of the sample was 8.0 ± 1.2 nm, revealing that the multilayers of the 2D PANI were stacked as shown in Fig. 4*B*. The pristine 2D PANI nanoflakes exhibited *n*-doped ambipolar behaviors with a Dirac point of -37 ± 3 V (Fig. 4*C*). Furthermore, the Ohmic contact behaviors between 2D PANI and source−drain electrodes were observed from the output curve (*SI Appendix*, Fig. S15). The average hole and electron mobilities were 0.047 ± 0.014 cm^2 V^{-1}·s^{-1} and 0.110 ± 0.019 cm^2 V^{-1}·s^{-1}, respectively.

Fig. 4*D* is the schematic diagram of the experimental setup for doping 2D PANI with HCl in a Pyrex glass container equipped with a dopant loading reservoir. After evacuating the chamber, 5 mL HCl [35% (wt/wt)] was injected into the dopant loading reservoir. Then the glass chamber was heated to various temperature ranges (20−160 °C) for 1 h to vaporize HCl for gaseous doping. The electrical properties of the FET devices were characterized inside a vacuum probe station. The conductivity of the pristine 2D PANI (undoped) was 0.72 ± 0.04 S/cm, whereas pristine linear PANI (undoped) is an insulator (*SI Appendix*, Table S3). After doping with HCl, 2D PANI showed dramatically increased electrical conductivity, as shown in Fig. 4*E*. With elevation of the doping temperature to 160 °C, the conductivity of the HCl-doped 2D PANI was increased as high as $1.41 \pm 0.06 \times 10^3$ S/cm, indicating that the electrical conductivity was increased by a factor of 1,960 after doping (Fig. 4*E*). This unprecedentedly high electrical conductivity of 2D PANI is approximately two orders of magnitude higher than the best performance of HCl-doped linear PANI reported to date (33). To the best of our knowledge, this value is the record high conductivity ever reported for PANI (*SI Appendix*, Table S3) (34). In addition, as 2D PANI was doped, field-effect behaviors disappeared, as shown in *SI Appendix*, Figs. S16 and S17. The Ohmic contact between 2D PANI and source−drain electrodes was also maintained with changing doping temperature (*SI Appendix*, Fig. S16). From these temperature-dependent doping experiments, the lowest temperature for optimizing the conductivity was found to be ~100 °C (Fig. 4*F*). Thus, 2D PANI can serve as a new class of soft 2D material with superior electrical properties.
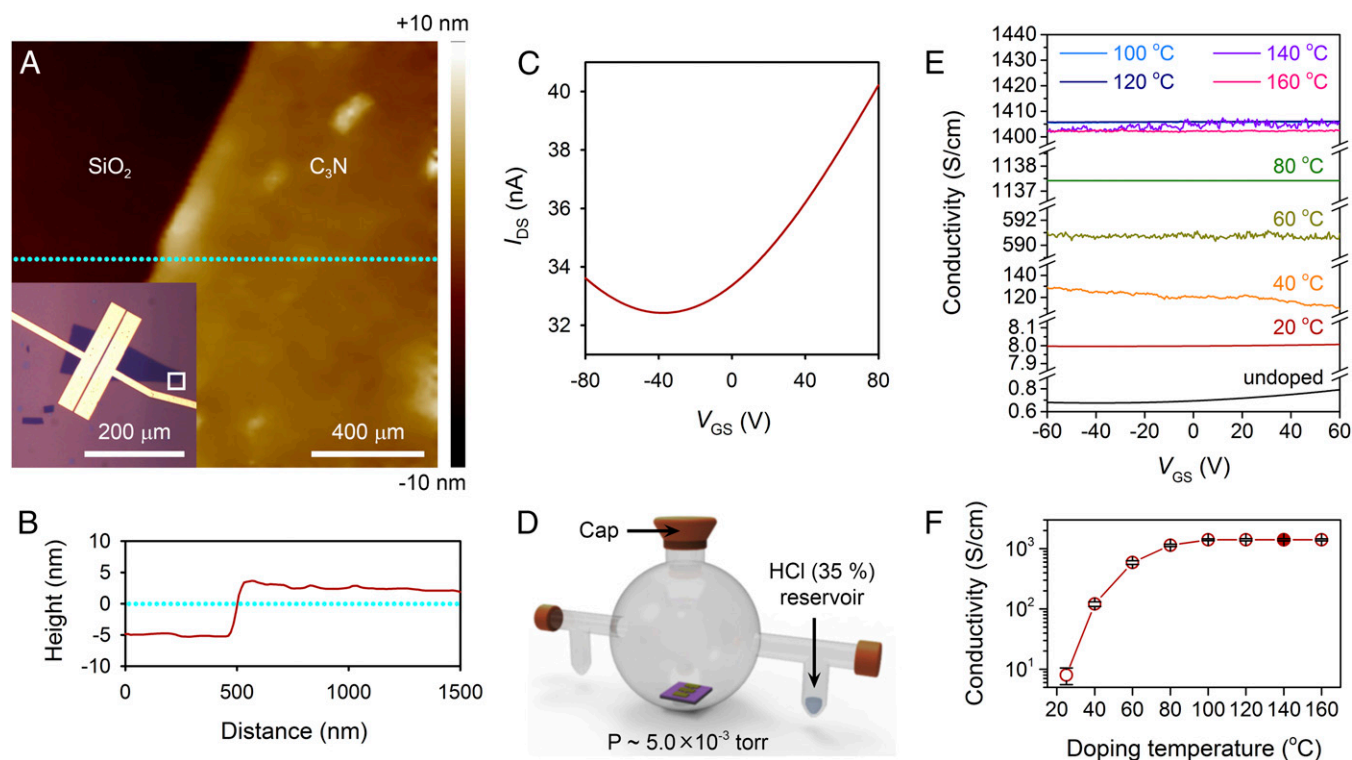
CHEMISTRY

Fig. 4. Electrical performance of 2D PANI and doping study with HCl gas. (*A*) AFM height image from the white square marked in *Inset*. *Inset* is optical microscope image of FET using 2D PANI as active material on Si wafer with 300 nm SiO_2. Source and drain (channel length = 500 nm) were patterned by e-beam lithography (W/L = 60 μm/0.5 μm = 120). (*B*) Thickness profile indicates a cross-section of the cyan-dashed line in *A*. (*C*) Transfer curve of pristine 2D PANI FET (without doping) as a function of gate voltage at V_{DS} = 10 mV, measured under vacuum (5×10^{-6} torr). (*D*) Schematic diagram of the doping setup for 2D PANI. (*E*) Conductivity changes as a function of gate voltage after doping with HCl gas. The solid black line represents the electrical property of the pristine 2D PANI (undoped). The doping temperature increased from 20 °C to 160 °C with a step of 20 °C. (*F*) Average conductivity (10 FET devices) changes as a function of the doping temperature.

In summary, we demonstrated a new synthetic protocol for 2D PANI, which can be produced by direct pyrolysis of organic HAB single crystals and has an empirical formula of C_3N (three sp^2 C atoms sharing a tertiary N) at basal area. The atomic-level true 2D PANI structure was realized for the first time, to our knowledge, as confirmed by STM imaging. Although DFT calculation suggested that 2D PANI had scant density of state at Fermi level as a metallic conductor, STS revealed the intrinsic electronic nature of 2D PANI with a HOMO–LUMO gap of 2.7 eV. Upon doping with gaseous HCl at an elevated temperature (~160 °C), the 2D PANI flakes exhibited electrical conductivity of 1.41×10^3 S/cm which, was two orders of magnitude higher than the best value of the doped linear PANI analogs reported to date. The structure of 2D PANI is quite striking, because it contains uniformly distributed nitrogen atoms for multifunctionality; hence, we expect that 2D PANI has strong potential, from wet chemistry to device applications, beyond graphene and its linear analog.

Materials and Methods

All of the chemicals and solvents were purchased from Sigma-Aldrich Chemical Inc. and used without further purification, unless otherwise specified.

Synthesis of HAB Trihydrochloride. 1,3,5-Triamino-2,4,6-trinitro-benzene (TATB) (3.0 g, 12 mmol) was placed in a high-pressure hydrogenation vessel with 10% Pd/C (0.5 g) and anhydrous ethyl acetate (150 mL) as a solvent. The reaction mixture was agitated under hydrogen (H_2) atmosphere (4.2 bar) until the yellowish colored TATB suspension completely disappeared. Then, concentrated HCl (100 mL) was added into the reaction vessel and further agitated under H_2 (4.2 bar) for an additional 5 h. The reaction mixture was then filtered under reduced pressure over Celite to remove the Pd/C catalyst. HAB trihydrochloride crystallized out nicely in quantitative yield

after washing of the Celite with 2M HCl. The precipitates were collected by suction filtration using polytetrafluoroethylene (PTFE) membrane (0.45 μm) and dried at 70 °C under reduced pressure overnight. To form high-quality single crystals, the white crystals (2.5 g) were dissolved again in deionized and degassed water (15 mL), filtered through PTFE membrane to remove solid impurities, if any, and concentrated HCl (80 mL) was added. The flask was tightly sealed and placed in a freezer until very large needle-type crystals developed (Fig. 1*B*).

Synthesis of 2D PANI Framework. Needle-type HAB crystals (white needles, 2.0 g) were taken in an aluminum oxide crucible and put in the furnace, and the chamber was degassed for five cycles of argon charge/discharge under reduced pressure (10^{-4} torr). Then, the furnace temperature was gradually increased to 500 °C (8 °C/min) under argon (10 cc/min) flow at reduced pressure for 2 h and maintained at 500 °C with continuous argon flow at reduced pressure (initial pressure: 4.5×10^{-4}; under argon: 1.9×10^{-3} torr). Then, it was slowly cooled to room temperature, and the sample was collected and Soxhlet extracted with water and methanol for 2 d each to remove soluble impurities, if any, yielding 770 mg (~quantitative) of black needles (Fig. 1*E*).

STM Experiments. The STM experiments were carried out in a UHV low-temperature STM (SPECS JT-STM) at 77 K. The Cu(111) single crystal was cleaned by a few cycles of Ar^+ sputtering and annealing. After cleaning the Cu(111) substrate, HAB crystal was deposited on the precleaned Cu(111) substrate by in situ thermal evaporation under UHV conditions. The sample evaporation temperature was about 600 K, and the temperature of the substrate was maintained at room temperature. To simulate the STM image, we integrated the Kohn–Sham charge density in the energy window of 0.7 eV below and above the Fermi level. The image shown in Fig. 3*D* is the conduction bands part of the charge density in the plane 1 Å about the atomic layer.

First-Principle Calculations. For computations, we used the Vienna Ab initio simulation package to calculate the ground state of many electrons

system in the framework of DFT (35–38). The plane wave basis set with an energy cutoff of 400 eV and the gradient-corrected exchange-correlation potential, formulated by Perdew et al. (39), was used. The ions were described by the projector augmented wave potentials. In the self-consistent-field total energy calculations, the k points are uniformly sampled over the reciprocal space of the 2D triangular lattice with mesh 21 by 21. All of the atomic positions of were relaxed within residual forces smaller than 0.01 eV/Å.

Fabrication of 2D PANI FET Devices. The 2D PANI crystalline films were fabricated by drop casting of the HAB crystals dissolved in trifluoromethanesulfonic acid on the preheated (140 °C) SiO_2 (300 nm)/Si substrate and subsequently heat-treated at 700 °C in argon atmosphere for 2 h. The thin flakes were transferred to fresh SiO_2 (300 nm)/Si substrate by PDMS stamping (32). Chromium (Cr, 4 nm) and gold (Au, 40 nm) were thermally evaporated. The source and drain electrodes were defined by e-beam lithography (channel length = 500 nm).

1. Runge FF (1834) Ueber einige produkte der steinkohlendestillation. *Anna Phys* 107(5): 65–78.
2. Brown OW, Frishe WC (1947) Catalytic oxidation of aniline in the vapor phase. *J Phys Colloid Chem* 51(6):1394–1400.
3. Macdiarmid AG, et al. (1985) "Polyaniline": Interconversion of metallic and insulating forms. *Mol Cryst Liquid Cryst* 121(1-4):173–180.
4. Stejskal J, Gilbert RG (2002) Polyaniline. Preparation of a conducting polymer (IUPAC Technical Report). *Pure Appl Chem* 74(5):857–867.
5. Chiang J-C, Macdiarmid AG (1986) 'Polyaniline': Protonic acid doping of the emeraldine form to the metallic regime. *Synth Met* 13(1-3):193–205.
6. MacDiarmid AG, Yang LS, Huang WS, Humphrey BD (1987) Polyaniline: Electrochemistry and application to rechargeable batteries. *Synth Met* 18(1-3):393–398.
7. Trivedi DC, Dhawan SK (1993) Shielding of electromagnetic interference using polyaniline. *Synth Met* 59(2):267–272.
8. Halvorson C, Cao Y, Moses D, Heeger AJ (1993) Third order nonlinear optical susceptibility of polyaniline. *Synth Met* 57(1):3941–3944.
9. Wang HL, MacDiarmid AG, Wang YZ, Gebier DD, Epstein AJ (1996) Application of polyaniline (emeraldine base, EB) in polymer light-emitting devices. *Synth Met* 78(1): 33–37.
10. Dutta D, Sarma TK, Chowdhury D, Chattopadhyay A (2005) A polyaniline-containing filter paper that acts as a sensor, acid, base, and endpoint indicator and also filters acids and bases. *J Colloid Interface Sci* 283(1):153–159.
11. Alam MM, Wang J, Guo Y, Lee SP, Tseng H-R (2005) Electrolyte-gated transistors based on conducting polymer nanowire junction arrays. *J Phys Chem B* 109(26): 12777–12784.
12. McCall RP, et al. (1991) Photoinduced absorption and erasable optical information storage in polyanilines. *Synth Met* 41(3):1329–1332.
13. Blinova NV, Stejskal J, Trchová M, Ciric-Marjanović G, Sapurina I (2007) Polymerization of aniline on polyaniline membranes. *J Phys Chem B* 111(10):2440–2448.
14. Tseng RJ, Huang J, Ouyang J, Kaner RB, Yang Y (2005) Polyaniline nanofiber/gold nanoparticle nonvolatile memory. *Nano Lett* 5(6):1077–1080.
15. Conway BE, Birss V, Wojtowicz J (1997) The role and utilization of pseudocapacitance for energy storage by supercapacitors. *J Power Sources* 66(1-2):1–14.
16. Bessière A, Duhamel C, Badot JC, Lucas V, Certiat MC (2004) Study and optimization of a flexible electrochromic device based on polyaniline. *Electrochim Acta* 49(12): 2051–2055.
17. Kalendová A, Veselý D, Stejskal J (2008) Organic coatings containing polyaniline and inorganic pigments as corrosion inhibitors. *Prog Org Coat* 62(1):105–116.
18. Prakash GKS, Suresh P, Viva F, Olah GA (2008) Novel single step electrochemical route to γ-MnO2 nanoparticle-coated polyaniline nanofibers: Thermal stability and formic acid oxidation on the resulting nanocomposites. *J Power Sources* 181(1):79–84.
19. Chang M-Y, et al. (2008) Polymer solar cells incorporating one-dimensional polyaniline nanotubes. *Org Electron* 9(6):1136–1139.
20. Mäkelä T, Sten J, Hujanen A, Isotalo H (1999) High frequency polyaniline shields. *Synth Met* 101(1-3):707.
21. Gao H, et al. (2004) Aqueous/ionic liquid interfacial polymerization for preparing polyaniline nanoparticles. *Polymer (Guildf)* 45(9):3017–3019.
22. Virji S, Huang J, Kaner RB, Weiller BH (2004) Polyaniline nanofiber gas sensors: Examination of response mechanisms. *Nano Lett* 4(3):491–496.
23. Ma Y, Zhang J, Zhang G, He H (2004) Polyaniline nanowires on Si surfaces fabricated with DNA templates. *J Am Chem Soc* 126(22):7097–7101.
24. Chaudhuri D, Datar S, Viswanatha R, Sarma DD, Amenitsch H (2005) Self-organization of polyaniline nanorods: Towards achieving a higher conductivity. *Appl Phys Lett* 87(9):093117.
25. Wei Z, Zhang Z, Wan M (2002) Formation mechanism of self-assembled polyaniline micro/nanotubes. *Langmuir* 18(3):917–921.
26. Li G, et al. (2004) Synthesis of polyaniline nanobelts. *Macromol Rapid Commun* 25(18): 1611–1614.
27. Han J, Song G, Guo R (2007) Nanostructure-based leaf-like polyaniline in the presence of an amphiphilic triblock copolymer. *Adv Mater* 19(19):2993–2999.
28. Ćirić-Marjanović G (2013) Recent advances in polyaniline research: Polymerization mechanisms, structural aspects, properties and applications. *Synth Met* 177:1–47.
29. Novoselov KS, et al. (2004) Electric field effect in atomically thin carbon films. *Science* 306(5696):666–669.
30. Geim AK, Novoselov KS (2007) The rise of graphene. *Nat Mater* 6(3):183–191.
31. Mahmood J, Kim D, Jeon I-Y, Lah MS, Baek J-B (2013) Scalable synthesis of pure and stable hexaaminobenzene trihydrochloride. *Synlett* 24(02):246–248.
32. Mahmood J, et al. (2015) Nitrogenated holey two-dimensional structures. *Nat Commun* 6:6486.
33. Choi IY, et al. (2015) High-conductivity two-dimensional polyaniline nanosheets developed on ice surfaces. *Angew Chem Int Ed Engl* 54(36):10497–10501.
34. Lee K, et al. (2006) Metallic transport in polyaniline. *Nature* 441(7089):65–68.
35. Hohenberg P, Kohn W (1964) Inhomogeneous electron gas. *Phys Rev* 136(3B): B864–B871.
36. Kohn W, Sham LJ (1965) Self-consistent equations including exchange and correlation effects. *Phys Rev* 140(4A):A1133–A1138.
37. Kresse G, Furthmüller J (1996) Efficient iterative schemes for ab initio total-energy calculations using a plane-wave basis set. *Phys Rev B Condens Matter* 54(16): 11169–11186.
38. Kresse G, Furthmüller J (1996) Efficiency of ab-initio total energy calculations for metals and semiconductors using a plane-wave basis set. *Comput Mater Sci* 6(1): 15–50.
39. Perdew JP, Burke K, Ernzerhof M (1996) Generalized gradient approximation made simple. *Phys Rev Lett* 77(18):3865–3868.

CHEMISTRY